



# Machine learning of Antarctic firn density by combining radiometer and scatterometer remote sensing data

Weiran Li<sup>1</sup>, Sanne B. M. Veldhuijsen<sup>3</sup>, and Stef Lhermitte<sup>1,2</sup>

<sup>1</sup>Department of Geoscience and Remote Sensing, Delft University of Technology, Delft, The Netherlands

<sup>2</sup>Department of Earth & Environmental Sciences, KU Leuven, Leuven, Belgium

<sup>3</sup>Institute for Marine and Atmospheric research Utrecht (IMAU), Utrecht, The Netherlands

**Correspondence:** Weiran Li (w.li-7@tudelft.nl)

**Abstract.** Firn density plays a crucial role in assessing the surface mass balance of the Antarctic ice sheet. However, our understanding of the spatial and temporal variations in firn density is limited due to i) spatial and temporal limitations of in situ measurements, ii) potential modelling uncertainties, and iii) lack of firn density products driven by satellite remote sensing data. To address this gap, this paper explores the potential of satellite microwave radiometer (SMISS) and scatterometer (AS-  
5 CAT) observations for assessing spatial and temporal dynamics of dry firn density over the Antarctic ice sheet. Our analysis demonstrates a clear relation between density anomalies at a depth of 4 cm and fluctuations in satellite observations. However, a linear relationship with individual satellite observations is insufficient to explain the spatial and temporal variation of snow density. Hence, we investigate the potential of a non-linear Random Forest (RF) machine learning approach trained on radiometer and scatterometer data to derive the spatial and temporal variations in dry firn density. In the estimation process,  
10 ten years of SSMIS observations (brightness temperature), ASCAT observations (backscatter intensity), and polarisation and frequency ratios derived from SSMIS observations are used as input features to a random forest (RF) regressor. The regressor is first trained on time series of modelled density and satellite observations at randomly sampled pixels, and then applied to estimate densities in dry firn areas across Antarctica. The RF results reveal a strong agreement between the spatial patterns estimated by the RF regressor and the modelled densities. The estimated densities exhibit an error of  $\pm 10 \text{ kg m}^{-3}$  in the  
15 interior of the ice sheet and  $\pm 20 \text{ kg m}^{-3}$  towards the ocean. However, the temporal patterns show some discrepancies, as the RF regressor tends to overestimate summer densities, except for high-elevation regions in East Antarctica and specific areas in West Antarctica. These errors may be attributed to underestimations of short-term (or seasonal) variations in the modelled density and the limitation of RF in extrapolating values outside the training data. Overall, our study presents a potential method for estimating unknown Antarctic firn densities using known densities and satellite parameters.

## 20 1 Introduction

Assessing firn properties of the Antarctic ice sheet is important for understanding the global climate system. For example, firn density, one of the commonly assessed firn properties, plays a key role in understanding the surface mass balance of the ice sheets (Kuipers Munneke et al., 2015) as it contributes to the interpretation of satellite altimetry measurements (Zwally et al., 2005; Schröder et al., 2019). In Antarctica, firn density is highly variable in space and time due to the varying surface



25 climate conditions (Craven and Allison, 1998; Li and Zwally, 2004; van den Broeke, 2008; Fujita et al., 2016). Therefore, it is necessary to continuously monitor firn density in Antarctica.

A variety of methods has been developed to assess firn density variations. In situ measurements from firn cores, snow pits and local near-infrared pictures are precious for accurately understanding firn densities (Macelloni et al., 2007; Picard et al., 2012; Champollion et al., 2013). However, these measurements are sparse in both space and time due to cost-efficiency considerations, making them insufficient for comprehensive monitoring requirements. In the absence of in situ data, firn densification models (FDMs), such as the semi-empirical IMAU-FDM (Ligtenberg et al., 2011; Veldhuijsen et al., 2023) are commonly utilised to estimate firn density and subsequent elevation changes (Schröder et al., 2019). Nonetheless, FDMs suffer from significant uncertainties (Verjans et al., 2020). For instance, the relationship between wind velocity and density, as derived by Sugiyama et al. (2012) and van den Broeke et al. (1999) exhibits notable discrepancies, introducing uncertainties when parameterising the effects of wind. Therefore, to obtain spatially and temporally continuous assessments of changes in firn densities, satellite remote sensing serves as an important complementary method (Picard et al., 2007; Brucker et al., 2014; Meredith et al., 2019). While numerous studies have investigated these assessments, they have identified intricate relationships between remote sensing observations and firn density, making it challenging to generalise remote sensing models. Consequently, a satellite-based firn density product remains elusive.

40 Among satellite remote sensing techniques, radiometers are a primary tool used for studying firn properties, offering various frequencies and polarisations that facilitate assessments of different firn properties at different depths (Picard et al., 2007, 2012; Champollion et al., 2013; Brucker et al., 2014). Radiometers measure the thermal radiation emitted by the ground surface and subsurface within the range of microwave penetration (Picard et al., 2007). The observed parameter is referred to as brightness temperature ( $T_B$ ), which has been typically used to derive Antarctic surface melting extent by detecting the sharp increase in emissivity and hence  $T_B$  (Picard et al., 2007; Tedesco, 2009; Nicolas et al., 2017; de Roda Husman et al., 2022). However, studies show that  $T_B$  can also be used to assess firn densities. For example, Champollion et al. (2013) used the temporal variation of polarisation ratio (horizontal/vertical) of  $T_B$  at 19 GHz and 37 GHz to evaluate the density changes of firn induced by hoar-crystal formation and disappearance. Alternatively, Tran et al. (2008) classified seven firn facies over Antarctica using a combination of  $T_B$ , a specific ratio defined by  $T_B$  at 23.8 GHz and 36.5 GHz, and Ku- and S-band altimeters. They attributed the different facies to varying surface roughness or firn grain size driven by differences in climate parameters such as wind patterns, firn accumulation, and temperature, which are known to influence firn density (Lehning et al., 2002; Champollion et al., 2013).

Alternatively, active microwave observations, specifically radar scatterometer and synthetic aperture radar (SAR), have been used to assess firn properties. The backscatter intensity ( $\sigma^0$ ) is a common parameter measured by both scatterometer and SAR. Numerous studies have been performed to link the spatial or temporal variation of  $\sigma^0$  to variations of certain firn properties. Fraser et al. (2016) analysed the drivers of spatial variation of  $\sigma^0$  using C-band scatterometer in dry firn zones of Antarctica. Their study concluded that (i) the seasonal variation of  $\sigma^0$  is primarily driven by precipitation and firn temperature, and (ii)  $\sigma^0$  exhibits a high correlation with long-term precipitation, whereas densities do not play a dominant role. On the other hand, Rizzoli et al. (2017) exploited interferometric acquisitions of X-band SAR  $\sigma^0$  from TanDEM-X, using the combination of



60  $\sigma^0$  and a volume correlation factor to classify Greenland into four firn facies. The firn facies classified by this study can be attributed to different melt extents.

The aforementioned studies highlight the capability of various passive and active satellite observations, either individually or in combination, to evaluate spatial and temporal patterns of firn density. However, the precise mechanisms underlying the interaction between firn densities and satellite observations cannot always be fully understood (Champollion et al., 2013; Fraser et al., 2016; Rizzoli et al., 2017). In addition, previous studies using satellite observations to assess firn properties are either restricted to a specific location where in situ measurements are available (Champollion et al., 2013) or to a specific time period. Generalisation of these techniques to other areas or time periods therefore requires further assessment (Tran et al., 2008; Fraser et al., 2016; Nicolas et al., 2017; Rizzoli et al., 2017). Hence, it is crucial to identify suitable combinations of satellite observables and data fusion methods that enable the assessment of firn density across extensive regions and multiple seasons, eliminating the necessity for frequent local calibration.

Consequently, the objective of this paper is to assess the feasibility of combining radiometer and scatterometer remote sensing data to assess Antarctica-wide dry firn density. To achieve this, we conduct a three-fold experiment involving the comparison of time series data from Special Sensor Microwave Imager/Sounder (SSMIS) and Advanced Scatterometer (ASCAT) satellites with in situ firn density measurements (SUMup) and the output of a semi-empirical firn densification model (IMAU-FDM). In the first experiment, we juxtapose the satellite time series with the output of IMAU-FDM to evaluate the potential of individual satellite parameters in linearly explaining density variations. The second experiment involves clustering analysis on the combined SSMIS and ASCAT satellite data to identify spatial and temporal patterns of satellite observations and compare them with IMAU-FDM patterns. Finally, we assess the potential of a non-linear Random Forest (RF) machine learning approach (Breiman, 1996, 2001) trained on SSMIS and ASCAT data to derive spatial and temporal variations in dry firn density.

## 2 Data

In this study, we evaluate the potential of satellite microwave radiometer (SMISS) and scatterometer (ASCAT) observations in assessing the spatial and temporal dynamics of dry firn density across the Antarctic ice sheet. We focus on the grounded Antarctic ice sheet only, where wet firn and melting that potentially affect the satellite microwave observations are less pronounced (Lenaerts et al., 2016; Kingslake et al., 2017; Spergel et al., 2021; Li et al., 2021; de Roda Husman et al., 2022). To account for this, we mask out all satellite observations over the ice shelves using the grounding line defined by Depoorter et al. (2013).

### 2.1 Radiometer data

Time series of brightness temperature ( $T_B$ ) from the Special Sensor Microwave Imager/Sounder (SSMIS) sensors are used in this study as they are widely used to assess variations in firn properties (Tedesco and Kim, 2006; Tran et al., 2008; Brucker et al., 2010). The available measurement channels include vertically and horizontally polarised 19 GHz, 37 GHz and 91.655 GHz,



and vertically polarised 22 GHz (Kunkee et al., 2008). However, for the purposes of this study, our focus is solely on the 19 GHz and 37 GHz channels, since the atmospheric influence is negligible at these frequencies (Picard et al., 2009; Brucker et al., 2011; Champollion et al., 2013). Theoretically, the penetration depths are 1–7 m (at 19 GHz) and 0.1–2 m (at 37 GHz) in  
95 Antarctica (Surdyk, 2002; Brucker et al., 2010). These characteristics ensure the possibility for SSMIS at 19 GHz and 37 GHz to monitor the changes of firn properties. The daily polar-gridded  $T_B$  data are acquired from the National firn and Ice Data Center (NSIDC) with a spatial resolution of 25 km for both the 19 GHz and 37 GHz channels (Meier et al., 2021). All data are acquired by the F17 sensor as it provides continuous daily data acquisition in the period between Jan. 1, 2011 and Dec. 31, 2020.

100 Besides the 19 GHz and 37 GHz  $T_B$  time series, we also derive the polarisation ratio and gradient ratio as they have been found to be associated with firn properties (Tran et al., 2008; Champollion et al., 2013). The polarisation ratio  $PR(f)$  and gradient ratio  $FR(p)$  are defined as

$$PR(f) = \frac{T_B(f, V)}{T_B(f, H)} \quad (1)$$

105 
$$FR(p) = \frac{T_B(19 \text{ GHz}, p)}{T_B(37 \text{ GHz}, p)} \quad (2)$$

where  $f$  corresponds to the 19 GHz or 37 GHz frequencies, respectively, and  $p$  corresponds to the different horizontal (H) and vertical (V) polarisations, respectively. It is important to note that we define  $PR(f)$  inversely to Champollion et al. (2013), who took the ratio of H over V. Therefore, in regions with possible hoar crystals which correspond to a low density, our  $PR(f)$  is expected to decrease instead of increase.

## 110 2.2 Scatterometer data

Backscatter intensity ( $\sigma^0$ ) from synthetic aperture radar (SAR) was also previously used to assess density variations due to the melting–refreezing process of certain firn types (Rizzoli et al., 2017) and to examine variations in firn facies (Fahnestock et al., 1993). In this study, we employ time series of  $\sigma^0$  from the Advanced Scatterometer (ASCAT) satellite sensor as an alternative to SAR  $\sigma^0$ , primarily due to its high temporal resolution (daily) and its coverage over the entire Antarctica. ASCAT  
115 is an operational C-band (5.255 GHz) fan-beam scatterometer (Figa-Saldaña et al., 2002; Fraser et al., 2016) that has been in operation on Metop satellites since 2006. It operates in V polarization and covers multiple incidence angles. For dry firn, penetration depth of C-band ASCAT is approximately 20 m (Rignot, 2002; Fraser et al., 2016). The ASCAT products used in this study are obtained from Brigham Young University (BYU) Microwave Earth Remote Sensing (MERS) laboratory (2010) (Long et al., 1993; Early and Long, 2001; Lindsley and Long, 2010). The data are processed using the scatterometer image  
120 reconstruction (SIR) algorithm, which enhances the spatial resolution of images from 25 km to 4.45 km. The processing of the products accounts for the incidence angle dependence of  $\sigma^0$ , as the measurements are made over multiple incidence angles. The  $\sigma^0$  is approximated as a linear function of incidence angle  $\theta$  in  $^\circ$  (Long and Drinkwater, 2000):

$$\sigma^0(\theta) = A + B(\theta - 40^\circ) \quad (3)$$



where  $A$  (in dB) is the  $\sigma^0$  normalised to  $40^\circ$ , and  $B$  (in  $dB/^\circ$ ) is a parameter describing the dependence of  $\sigma^0$  on  $\theta$ . In this study,  
125 we only use the isotropic, normalised  $A$  parameter (hereafter  $\sigma^0$ ) as it has been shown to better correlate with various climate  
parameters (Fraser et al., 2016). To ensure consistent analysis between  $T_B$  and  $\sigma^0$ , the BYU  $\sigma^0$  products are interpolated to the  
same polar grids as the SSMIS  $T_B$  products. The data acquisition time is the same as that of the radiometer data.

### 2.3 Densities from Firn Densification Model

To understand the spatio-temporal variation in satellite data, we compare the SMISS and ASCAT satellite data to the output of a  
130 semi-empirical firn densification model. Therefore, we use output from the latest version of the IMAU Firn Densification Model  
(IMAU-FDM v1.2A; Veldhuijsen et al. (2023)). IMAU-FDM simulates the transient evolution of the Antarctic firn column,  
and is forced at the upper boundary by outputs of the regional atmospheric climate model RACMO2.3p2 (van Wessem et al.,  
2018). The density of the freshly fallen snow is a function of instantaneous wind speed and temperature in IMAU-FDM. Over  
time, the simulated firn layers become denser due to dry-snow densification and meltwater refreezing.

135 For the comparison with satellite observations, we focus on the density of the top 4 cm ( $\rho_{4cm}$ ) and the top 1 m ( $\rho_{1m}$ ) from  
the model output. We also use  $\rho_{4cm}$  for density estimation using the random forest (RF) regressor. The choice of the 4 cm  
depth is based on the fact that many in situ measurements used for evaluating the density estimations have been acquired at  
approximately this depth. The selection of the 1 m depth serves as a compromise between the expected penetration depths at  
19 GHz and 37 GHz.

140 The unrealistically large values in  $\rho_{4cm}$  (more than  $1000 \text{ kg m}^{-3}$ ) are treated as invalid. The firn data from the model are  
provided at a temporal resolution of 10 days and have a spatial resolution of 27 km. To facilitate comparison with the satellite  
products, the firn data are reprojected to the same polar grids as the satellite data.

### 2.4 Reference in situ density measurements

Furthermore, we employ in situ density measurements obtained from the Surface Mass Balance and Snow on Sea Ice Working  
145 Group (SUMup) dataset (Koenig and Montgomery, 2018; Montgomery et al., 2018) as a reference for spatial evaluation of  
the satellite data and the RF regressor. For each date of measurement at each location, density measurements at the smallest  
mid-point depths are used. Such depths are also restricted to  $< 1$  m. The measurements within the depth restriction were taken  
between Jan. 22, 1984 and Jan. 23, 2017, and consist of 124 points. The SUMup dataset does not contain time series, but  
only single measurements on specific dates. Therefore, we use the SUMup dataset only for spatial evaluation of the potential  
150 uncertainties from both the IMAU-FDM densities and the densities estimated by the RF regressor.

In addition to the spatial evaluation, a temporal comparison between the IMAU-FDM densities and in situ densities can be  
performed at Dome C using the dataset from Leduc-Leballeur et al. (2017) available at Leduc-Leballeur et al. (2021). The  
measurements were taken between Oct. 7, 2014 and Jun. 1, 2015 at the depth of 0 – 2 cm. The discrete measurements are  
interpolated to create a continuous time series for visual analysis.



## 155 2.5 ERA5 climate parameters

To assess the difference between the measured, modelled and estimated densities, it is important to understand the effects of climate conditions. Therefore, we use ERA5 wind speed and surface temperature estimated at midday (Copernicus Climate Change Service, 2019) as an approximation of the daily weather conditions. By incorporating this information, we aim to better interpret the discrepancies between the observed and modeled densities, as well as the discrepancies between the modeled  
160 densities and the densities estimated from satellite observations. The ERA5 wind speed and surface temperature data have a horizontal resolution of 9 km. Similarly to the IMAU-FDM data, we interpolate these climate variables to the same polar grids as the SSMIS data to ensure consistency in the analysis.

## 3 Method

We assess the potential of SSMIS and ASCAT satellite observations to assess dry firn density in a three-fold experiment. First,  
165 we compare the satellite time series with the output of IMAU-FDM to evaluate the potential of individual satellite parameters to linearly explain density variations (Section 3.1). Second, we perform clustering analysis on the combined SSMIS and ASCAT observations to identify spatio-temporal patterns of satellite observations. These patterns are then compared with the patterns obtained from IMAU-FDM, and dry-snow zones are determined (Section 3.2). Finally, we quantify the potential of a non-linear Random Forest (RF) machine learning approach trained on SSMIS and ASCAT observations to derive the spatial and temporal  
170 variations in dry firn density (Section 3.3).

### 3.1 Calculation of correlation between satellite parameters and firn density

To gain a general understanding of the spatial patterns of the satellite parameters and densities from IMAU-FDM, we calculate and visualise the map of  $T_B$ ,  $\sigma^0$ ,  $PR(f)$ ,  $FR(p)$  and 4 cm and 1 m firn densities ( $\rho_{4cm}$  and  $\rho_{1m}$ ) averaged between Jan. 1 2011 and Dec. 31 2020. Then, to observe the temporal correlation between the satellite parameters and the IMAU-FDM densities,  
175 for each pixel, the correlation coefficient between different satellite parameters and the firn density (at 4 cm for simplification) over time is calculated and visualised. To ensure consistent temporal resolution for the analysis, the satellite parameters are downsampled from daily resolution to 10-day resolution to match the temporal resolution of the IMAU-FDM densities.

### 3.2 Characterisation of firn types using time series of microwave observations

Spatial clustering of satellite observations (e.g.  $T_B$  and  $\sigma^0$ ) and products derived from satellite observations (e.g. ratio of  $T_B$   
180 used by Tran et al. (2008) and volume decorrelation used by Rizzoli et al. (2017)) is typically performed to characterise firn facies for further interpretation of spatio-temporal variations of firn properties, when in situ measurements are not sufficient to perform a supervised classification (Tran et al., 2008; Rizzoli et al., 2017). In our study, the spatial clustering of satellite observations is primarily carried out as a preparatory step aiming at ensuring that all the representative regions, i.e. the regions with distinctive satellite data patterns, are correctly accounted for into the model training procedure. By performing spatial



185 clustering, we aim to capture the diversity of satellite data patterns and incorporate them into the subsequent analysis. This step facilitates a comprehensive understanding of the spatio-temporal variations of firn properties based on the available satellite observations. To estimate the density between Jan. 1 2011 and Dec. 31 2020 using the RF regressor, pixels with melt events should be ruled out, as meltwater contents largely affect  $T_B$  and  $\sigma^0$  (Fahnestock et al., 1993; Brucker et al., 2010), rendering density estimations invalid in such cases. We anticipate that clustering the time series of satellite observations will effectively  
190 distinguish melting pixels from those that do not experience melt. By identifying and excluding melt-affected pixels, we can ensure the validity of density estimations using the RF regressor. Furthermore, to ensure that the RF regressor captures the characteristics of different dry snow types, we select training samples based on the identified dry snow types. This approach allows for the representation of various snow types within the training dataset, enhancing the ability of the RF regressor to estimate density accurately across different snow types.

195 Since  $T_B$  is strongly dependent on seasonal variations of firn temperature, the average seasonal signal is removed in the clustering process to obtain time series anomalies that reflect the variations of other properties. In addition, although  $\sigma^0$  may not have such large dependence on firn temperature as  $T_B$ , we use its time series anomalies to maintain consistency with  $T_B$ . The time series anomalies are calculated by taking the ten-year average of  $T_B$  or  $\sigma^0$  for each day in a year, defined as  $\bar{T}_B$  and  $\bar{\sigma}^0$ , and subtracting this averaged time series from the absolute observations for each year, leading to  $T_{B\text{anom}} = T_B - \bar{T}_B$  and  
200  $\sigma_{\text{anom}}^0 = \sigma_B - \bar{\sigma}^0$ . The time series anomalies of  $T_{B\text{anom}}$  and  $\sigma_{\text{anom}}^0$  are then normalised and stacked for clustering.

The adopted clustering solution is a simple hierarchical algorithm (Ward, 1963) which uses the  $T_{B\text{anom}}$  and  $\sigma_{\text{anom}}^0$  time series as input. For pre-processing, we remove outliers in the time series per pixel by defining an interval of three standard deviations above and below average. Then, the temporal gaps are filled with a linear interpolation. The clustering algorithm requires the number of clusters as input, which should be based on a selected threshold of the ‘distance’ between pixels. The  
205 distance is calculated as the variance between the parameters of different pixels. The threshold can be determined based on a dendrogram where each branch of the clustering algorithm represents pixels that have the smallest distance between each other. The number of clusters is then defined based on the criteria that ensures a sufficient number of clusters and sufficient spacing between the higher and lower hierarchies. After visual inspection of the dendrogram and experiment with 5, 6, and 7 clusters, we select 7 clusters as the optimal clustering for the active and passive microwave satellite time series of the Antarctic ice sheet.  
210 Following the clustering process, we visualise the mean, 20th percentile, and 80th percentile of different satellite parameters, together with the IMAU-FDM density for each cluster. This allows a comparison of the changes in satellite observations with density variations across the clusters.

### 3.3 Deriving firn densities using satellite parameters and random forest regressor

Given the complex and often non-linear relationships between satellite observations and firn density (Fraser et al., 2016), a  
215 non-linear regression model based on machine learning is explored to relate the satellite time series to firn density. The method relies on a certain amount of known density measurements as the training dataset, and on the continuous satellite parameters as the trained features. We opt for a random forest regressor as machine learning model (RF regressor hereafter), as it can avoid



overfitting or underfitting by hyperparameter tuning, and can facilitate the interpretation of results by providing the importance of features.

220 Ideally, in situ measurements should be used as the training dataset. However, in situ measurements are often single measurements that lack temporally continuous observations. As our goal is to relate the satellite time series to assess spatio-temporal variations in firn density, we adopt an alternative approach that uses the output of IMAU-FDM as training data instead of relying on in situ data. Although this approach has the disadvantage of training the RF regressor on a noisy IMAU-FDM dataset, which may exhibit spatial and temporal differences compared to actual in situ densities (e.g., biases between the model and in situ  
225 observations), we leverage the strengths of random forest regression for pattern recognition in noisy datasets. The use of multiple decision trees and random feature selection can reduce the variance of the model and prevent overfitting, resulting in better generalisation performance on noisy data. Additionally, the ability to estimate feature importance allows for identification of relevant features, which can further improve performance on noisy data. Therefore, we expect that the RF regressor generalises on the density estimations of IMAU-FDM, which is known to capture the spatial variation of in situ density measurements well  
230 and the temporal variations reasonably well (Veldhuijsen et al., 2023).

The training, testing, and implementation of the RF regressor involve three main steps:

- Training and Hyperparameter Tuning: a subset of IMAU-FDM densities (Subset I) is used as the training dataset in a 5-fold cross-validation procedure. Multiple models are evaluated, representing different combinations of hyperparameters defined for the RF regressor (see Table 1). The goal is to identify the configuration that achieves the best cross-validation  
235 score, indicating the optimal set of hyperparameters for the RF regressor.
- Testing and Model Evaluation: a different subset of IMAU-FDM densities (Subset II) is used as input to the RF regressor, which has been trained on Subset I. The purpose of this step is to evaluate the performance of the model and assess the accuracy of the RF density estimations. Additionally, it helps to determine the importance of satellite parameters in the predictions of the regressor.
- 240 – Antarctica-wide Implementation: The satellite time series covering the entire study area are fed into the RF regressor, which has been trained on Subset I. This step aims to estimate densities across the entire Antarctic dry-firn region. The output densities are then evaluated by comparing them to both the IMAU-FDM densities and the SUMup densities.

Both Subset I and Subset II consist of 100 randomly selected pixels from the non-melting pixels clustered in Section 3.2. These pixels are chosen from the period between January 1, 2011, and December 31, 2020, resulting in 3,653 samples in total  
245 for each pixel. The number of pixels selected from each cluster is proportional to the number of pixels in that cluster, ensuring representation from all clusters.





**Table 1.** Hyperparameter range and optimal values used to specify the random forest (RF) model. None indicates that the maximum tree depth is not restricted (i.e. all leaves at a node contain fewer samples than the minimum number of samples defined). All indicates that all features are considered when searching for the best split.

Parameter	Hyperparameter range	Optimal hyperparameter value
Number of trees	90, 100, 110	90
Maximum depth of the tree	None, 6, 7, 8, 9	9
The minimum number of samples at a leaf node	1, 3, 5, 7, 9	5
The number of features to consider when searching for the best split	3, 4, 5, 6, 7, All	3

The RF regressor is implemented with the target variable  $\rho_{Acm}$  and input features  $\mathbf{X}$  defined as follows:

$$\mathbf{X} = (T_B(19V), T_B(19H), T_B(37V), T_B(37H), \sigma^0, T_{B_{anom}}(19V), T_{B_{anom}}(19H), T_{B_{anom}}(37V), T_{B_{anom}}(37H), \sigma_{anom}^0, PR(19GHZ), PR(37GHZ), FR(V), FR(H)) \quad (4)$$

Within  $\mathbf{X}$ , we include  $T_B$  and  $\sigma^0$  to account for variations in temperature, precipitation and other potential climate parameters that show a potential strong seasonality (e.g., Fraser et al., 2016), whereas the anomalies in  $T_B$ ,  $\sigma^0$ ,  $PR$  and  $FR$  are included to account for temporal and spatial variations relative to the seasonal cycle. Moreover, we exclude melting pixels from the RF regressor as melt potentially disturbs the satellite parameters. To ensure consistent temporal resolution between the input features and the target IMAU-FDM densities, the daily satellite parameters are also downsampled to the 10-day temporal resolution of the IMAU-FDM firn density by selecting the corresponding acquisition date.

In the testing and evaluation step, we assess the performance of the optimal RF regressor. This is achieved by comparing the RF and IMAU-FDM densities of Subset II using scatterplots and standard evaluation metrics, i.e. the root mean square error (RMSE) between the RF densities and the IMAU-FDM densities. The importance of satellite parameters in the RF regressor is computed by calculating the Gini importance. Gini importance in RF regression is a measure of feature importance based on the Gini impurity index. It measures how much each feature contributes to the reduction in variance of the model when that feature is used for splitting the data. Features with higher Gini importance are considered more important for the predictive performance of the model (Archer and Kimes, 2008).

Finally, in the Antarctic-wide implementation, the optimal RF regressor is implemented to predict the spatial and temporal variations in firn density. These predictions are then compared with IMAU-FDM and the SUMup densities. The spatial agreement is assessed by comparing the temporal averages of the RF predictions, IMAU-FDM and SUMup by means of the RMSE. The temporal agreement is assessed by the RMSE between the per-pixel time series of RF predictions and IMAU-FDM predictions and the coefficient of determination ( $R^2$ ) of their linear fit. We also compare the spatial patterns of the RF-predicted densities with the ERA5 climate parameters of surface temperature and wind velocity as these are potential drivers for spa-



tial variation in firn density. Finally, we illustrate this temporal agreement by showing time series over eight random pixels and Dome C (E in Fig. 3), where extensive studies have been performed (Champollion et al., 2013; Brucker et al., 2014; 270 Leduc-Leballeur et al., 2017).

## 4 Results

### 4.1 Correlation between satellite parameters and firn density

Figure 1 displays the averaged maps of satellite parameters,  $\rho_{4cm}$  and  $\rho_{1m}$ . The figure shows that, although all satellite parameters reflect some of the spatial patterns of firn density, none of the parameters shows a spatially consistent relation with  $\rho_{4cm}$ . 275 For example, in high-elevation regions of East Antarctica, firn densities,  $PR(f)$ , and  $FR(p)$  show similar or reversed broad-scale spatial patterns. However, these patterns are not consistently observed in most coastal regions, along the Transantarctic Mountains, and in cluster Firn 5 (Figure 3), where a significant melt event in 2016 affected the satellite observations (Nicolas et al., 2017).

The lack of spatial and temporal consistency between satellite and density is also illustrated in Fig. 2, which shows the pixel-wise temporal correlation of each satellite parameter with the 4 cm density in IMAU-FDM. All  $T_B$  channels generally show 280 a positive correlation with  $\rho_{4cm}$  in East Antarctica, but a negative correlation in West Antarctica and many coastal regions. Vertical polarisation  $T_B$  shows higher correlations compared to horizontal polarisation. Contrary to the findings of Champollion et al. (2013),  $PR(f)$  does not show a consistently positive correlation with  $\rho_{4cm}$ , especially at the location of Dome C, where the correlation coefficient between  $\rho_{4cm}$  and  $PR(19GHz)$  is -0.25, and between  $\rho_{4cm}$  and  $PR(37GHz)$  is -0.29. Most pixels 285 show a negative correlation between  $\rho_{4cm}$  and  $FR(p)$ , except for coastal regions that show positive correlation. Finally, the correlation between  $\rho_{4cm}$  and  $\sigma^0$  is generally low, except for the Firn 5 region, where the correlation coefficient is up to 0.5.

Overall, this correlation analysis indicates that the relationship between satellite parameters and firn density is complex, and simple linear relationships cannot adequately describe the IMAU-FDM density based on different satellite parameters. Therefore, non-linear approaches such as the RF regressor should be employed to assess the potential of relating the IMAU- 290 FDM firn density to various satellite parameters.

### 4.2 Firn-type clusters

Figure 3 shows the map of clusters derived from time series of the combined satellite parameters, where each cluster represents a natural grouping of pixels with similar satellite time series behaviour. The map shows that four large clusters (referred to as Firn 1–4) cover the dry firn interior of Antarctica. Firn 1–3 in East-Antarctica and Firn 4 in West-Antarctica. Firn 5 is a cluster 295 in West Antarctica close to Ross Sea which corresponds to the region that showed a strong melt event in Jan. 2016 (Nicolas et al., 2017) while Firn 6 and Firn 7 show small regions near the coastline in East- and West-Antarctica respectively that also show clear melting signals.

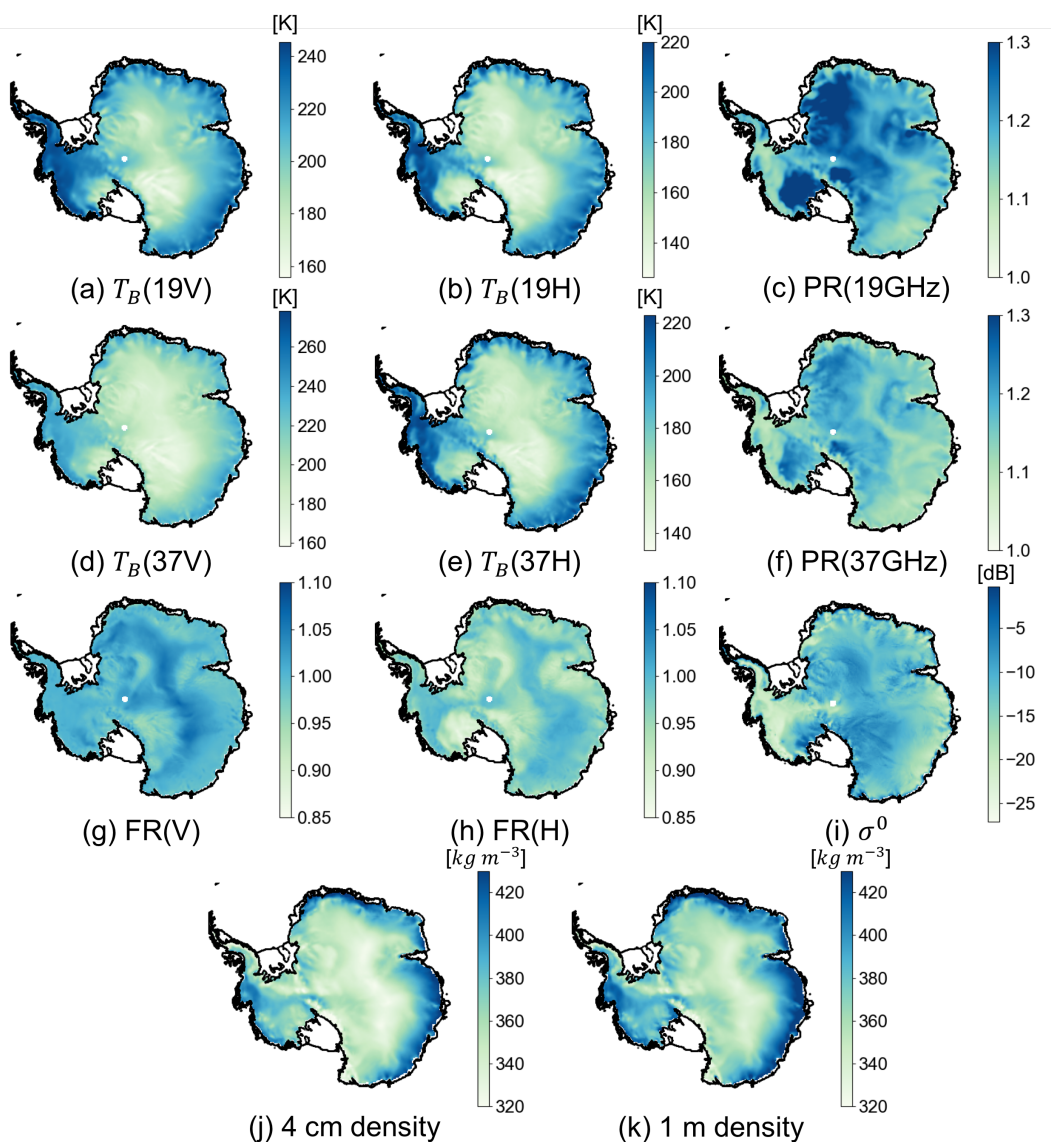


**Figure 1.** Temporally averaged map of (a) brightness temperature ( $T_B$ ) from 19 GHz vertical polarisation, (b)  $T_B$  from 19 GHz horizontal polarisation, (c) polarisation ratio from 19 GHz ( $PR(19 GHz)$ ), (d)  $T_B$  from 37 GHz vertical polarisation, (e)  $T_B$  from 37 GHz horizontal polarisation, (f) polarisation ratio from 37 GHz ( $PR(37 GHz)$ ), (g) frequency ratio from vertical polarisation ( $FR(V)$ ), (h) frequency ratio from horizontal polarisation ( $FR(H)$ ), (i) backscatter intensity ( $\sigma^0$ ), (j) 4 cm IMAU-FDM density ( $\rho_{4cm}$ ) and (k) 1 m IMAU-FDM density ( $\rho_{1m}$ ). The coastline is from Depoorter et al. (2013).

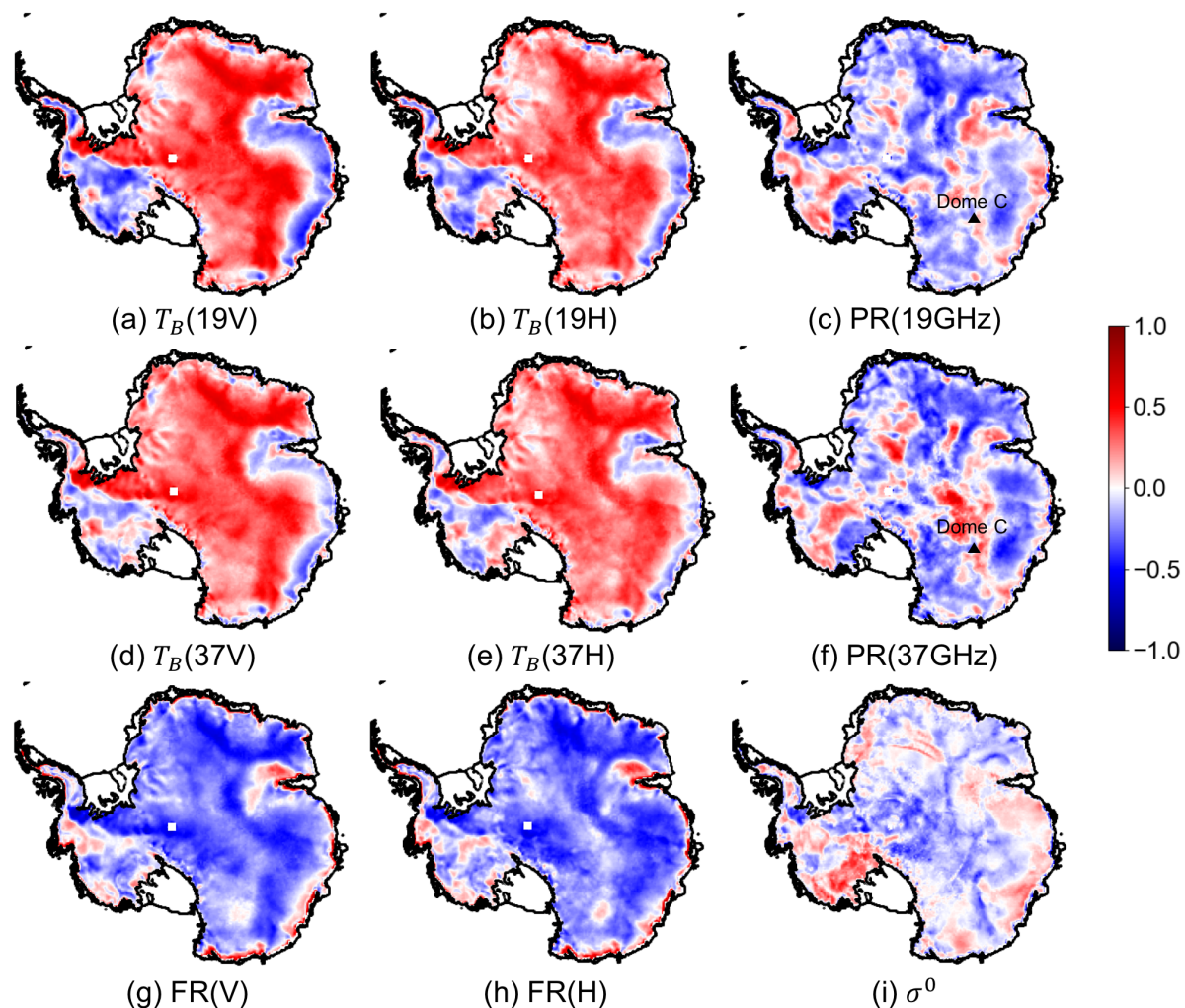


**Figure 2.** Map of temporal correlation calculated per pixel between 4 cm IMAU-FDM density and (a) brightness temperature ( $T_B$ ) from 19 GHz vertical polarisation, (b)  $T_B$  from 19 GHz horizontal polarisation, (c) polarisation ratio from 19 GHz ( $PR(19GHz)$ ), (d)  $T_B$  from 37 GHz vertical polarisation, (e)  $T_B$  from 37 GHz horizontal polarisation, (f) polarisation ratio from 37 GHz ( $PR(37GHz)$ ), (g) frequency ratio from vertical polarisation ( $FR(V)$ ), (h) frequency ratio from horizontal polarisation ( $FR(H)$ ), and (i) backscatter intensity ( $\sigma^0$ ). The coastline is from Depoorter et al. (2013).

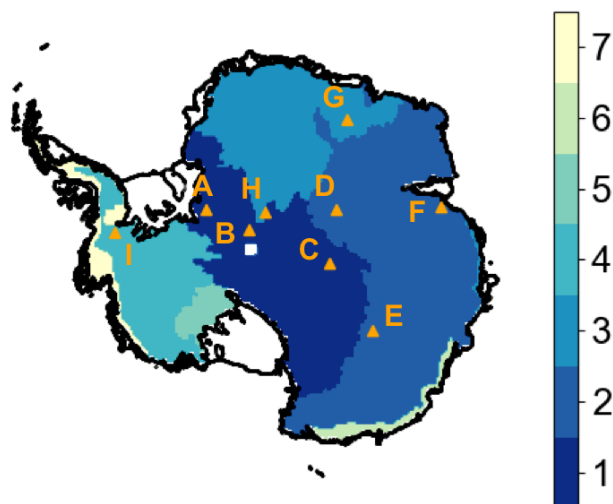


**Figure 3.** Clustering results from the combination of normalised  $T_B$  and  $\sigma^0$  after removing the seasonal trend. Triangles show the locations where temporal assessment per pixel is performed. The coastline is from Depoorter et al. (2013).

Figure 4 presents the time series of the mean and 20th–80th percentiles of each parameter for each cluster, (a)–(g) corresponding to clusters 1–7, respectively. Clusters Firm 1–4 exhibit small and short-term variations in  $T_{Banom}$  and  $\sigma^0_{anom}$ , with fluctuations of approximately  $\pm 5$  K and  $\pm 0.5$  dB, respectively, while their  $PR(f)$  and  $FR(p)$  time series undergo regular and similar seasonal cycles. The differences between these clusters mainly arise from deviations in  $T_{Banom}$  and, to a lesser extent,  $\sigma^0_{anom}$ . On the contrary, clusters Firm 5–7 all show large and abrupt variations in  $T_{Banom}$  and  $\sigma^0_{anom}$ , mainly as a result of melt events (e.g., Nicolas et al., 2017) that drastically change absorption, emission and scattering of microwave radiation and thus the  $T_{Banom}$  and  $\sigma^0_{anom}$ . The effects of these melt events are also evident in the time series of  $PR(f)$ ,  $FR(p)$ , and the IMAU-FDM densities, as the abrupt changes in firn density are associated with the occurrence of melt events. For example, this can be clearly seen in the time series of cluster Firm 5, where the melt event of 2016 shows a prolonged effect on the  $\sigma^0_{anom}$  time series due to the formation of a sub-surface refrozen high-density layer in IMAU-FDM. The high-density layer is detected by the scatterometer with stronger snow penetrating capability. In IMAU-FDM, this high density layer appears both in  $\rho_{4cm}$  where it disappears after a year (and a new high density layer forms in 2017) and in  $\rho_{1m}$  where the increase in density is apparent throughout multiple years. The comparison of all clusters highlights the dominant influence of melt events on  $T_{Banom}$  and  $\sigma^0_{anom}$  in the wet-firn pixels, whereas the dry-firn pixels exhibit a more pronounced seasonal variation in satellite parameters. It is important to note that the wet firn clusters are not used in the following RF steps due to the complex impact of the melt–refreeze cycle on satellite observations.

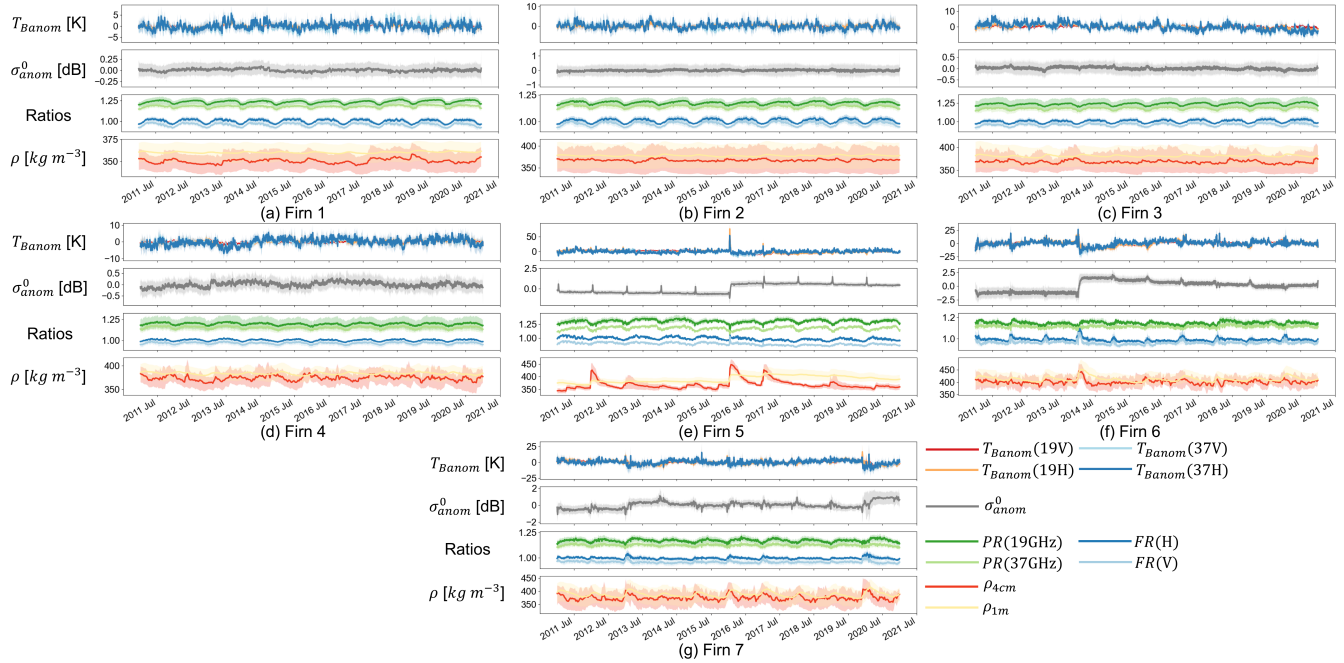


**Figure 4.** Time series of mean (curves) and 20th–80th percentiles (shaded areas) of the clustering results in Fig. 3, (a)–(g) corresponding to Snow facies 1–7. The visualised satellite observations are: time series anomalies of brightness temperature ( $T_B$ ) from 19 GHz and 37 GHz, both horizontal and vertical polarisation ( $T_{B_{anom}}(19V)$ ,  $T_{B_{anom}}(19H)$ ,  $T_{B_{anom}}(37V)$  and  $T_{B_{anom}}(37H)$ , respectively), polarisation ratio from 19 GHz ( $PR(19GHz)$ ) and 37 GHz ( $PR(37GHz)$ ), frequency ratio from vertical polarisation ( $FR(V)$ ) and horizontal polarisation ( $FR(H)$ ), time series anomalies of backscatter intensity ( $\sigma_{anom}^0$ ), and IMAU-FDM density at 4 cm ( $\rho_{4cm}$ ) and at 1 m ( $\rho_{1m}$ ) depths. The colours of the curves correspond to the legends in (g).

### 4.3 Assessment of RF densities at sample pixels

315 Figure 5a presents the results of the RF regressor for estimating firn densities based on satellite parameters. It demonstrates  
 that the non-linear multivariate approach of the RF regressor captures the spatial variations in IMAU-FDM density, exhibiting  
 a linear relationship between predictors and the predicted variable with a slope of 0.54. The RMSE is  $18.89 \text{ kg m}^{-3}$  and  $R^2$   
 is 0.49. Moreover, the RF regressor performs most ideally between approximately  $330 \text{ kg m}^{-3}$  and  $360 \text{ kg m}^{-3}$ , whereas it  
 fails to capture the large densities as no RF estimate exceeds  $410 \text{ kg m}^{-3}$ , which can be due to a well-known extrapolation  
 320 problem intrinsic to the RF regression (Hengl et al., 2018). The feature importance provided by Gini impurity index (Fig. 5b)  
 shows the ranked importance of satellite parameters in the predictive performance of the model, indicating that the raw  $T_B$  and  
 $\sigma^0$  observations are more important than the  $PR$  and  $FR$  ratios or the anomalies in predicting the  $\rho_{4cm}$ . The dominance of  $T_B$   
 is understandable as both  $T_B$  and  $\rho_{4cm}$  are dependent on firn temperature. This correlation is also clearly visible in Fig. 2. We  
 attribute the high importance of  $\sigma^0$  to the fact that it can be influenced by other  $\sigma^0$  parameters that have an impact on dry-snow

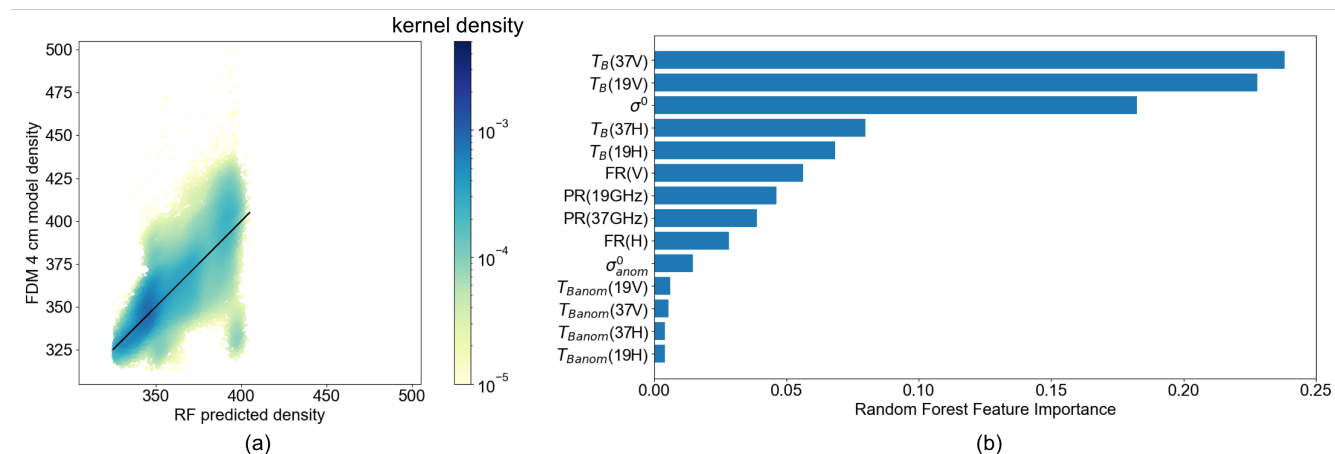


**Figure 5.** (a) Density comparison between RF densities and IMAU-FDM densities at sample pixels referred to as Subset I, the colour of the points showing the spatial density of points nearby; the colour bar is in logarithmic scale, and (b) feature importance of different input satellite parameters.

325 scattering properties, such as wind and precipitation; the mechanism may not necessarily be linear, but rather complex (Fraser et al., 2016). Among the derived satellite observations ( $PR(f)$  and  $FR(p)$ ),  $FR(V)$  has the highest importance. The  $T_B$  time series anomalies overall show little importance, which can also be observed in Fig. 4, where the  $T_B$  time series anomalies are mainly high-frequency signals that do not correspond to changes in densities in dry-firn regions.

#### 4.4 Spatial assessment of RF densities

330 In Figure 6, the temporally averaged RF density estimates and their differences relative to IMAU-FDM densities at the 4 cm depth and SUMup in situ densities are presented. The comparison in Fig. 6c shows that temporally averaged RF density estimations are in general larger than temporally averaged IMAU-FDM density in interior regions of Antarctica except for megadune regions, whereas they are lower towards coastal regions. The RMSE between the IMAU-FDM and RF averages (referred to as FDM-RF) is  $17.61 \text{ kg m}^{-3}$  and the mean FDM-RF difference is  $3.19 \text{ kg m}^{-3}$ . Meanwhile, the comparison with  
 335 the SUMup densities shows that RF and IMAU-FDM densities have comparable error patterns. The RMSE of FDM-SUMup is  $57.96 \text{ kg m}^{-3}$ , and the mean of FDM-SUMup bias is  $20.32 \text{ kg m}^{-3}$ ; the RMSE of RF-SUMup is  $64.43 \text{ kg m}^{-3}$ , and the mean of RF-SUMup is  $26.17 \text{ kg m}^{-3}$ . This shows a general overestimation and a large bias of both IMAU-FDM and the RF models when validated with the SUMup measurements. In Fig. 6d, it can be observed that neither IMAU-FDM nor RF manages to follow the large SUMup dynamics. This difference between models and in situ measurements can be attributed to the temporal  
 340 discrepancies between the measurements and the IMAU-FDM and satellite observations, and the IMAU-FDM model errors or uncertainties that can also be learned by the RF regressor.

Aided by Figure 7, we then analyse the temporal distribution of the offsets between the IMAU-FDM densities and the RF densities in more depth. Figure 7a generally shows low RMSE between IMAU-FDM and RF densities in high-elevation

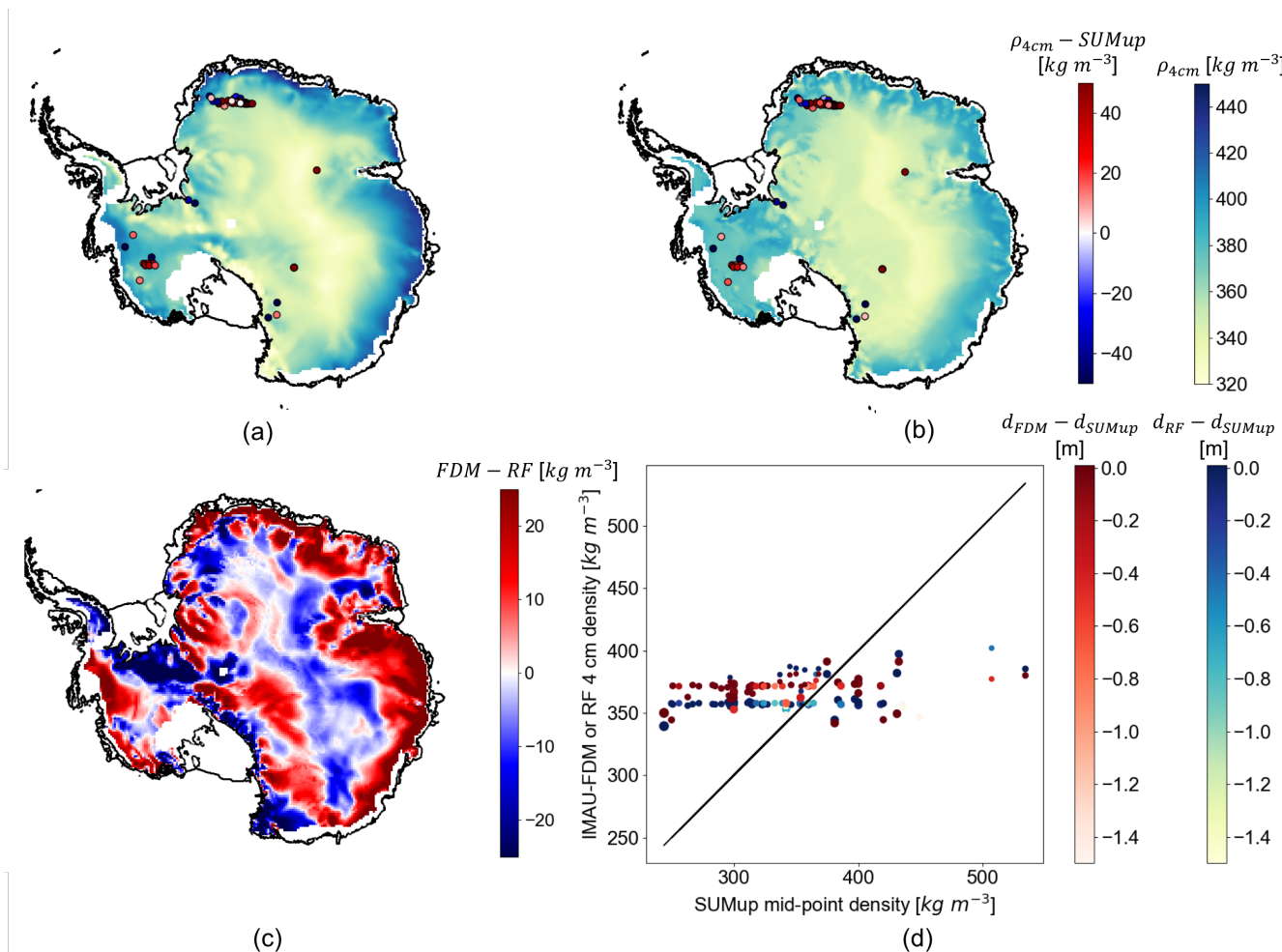


**Figure 6.** (a)–(c) Map of (a) temporally averaged IMAU-FDM 4 cm densities, (b) temporally averaged RF densities, (c) difference between averaged IMAU-FDM densities and RF densities ( $FDM - RF$ ). Difference between the modelled or estimated densities and the SUMup densities are shown in scattered points in (a) and (b) as FDM-SUMup or RF-SUMup. (a) and (b) share the same colour bar, in which blue–red shows the difference between the IMAU-FDM or RF densities and the SUMup densities ( $\rho_{4cm} - SUMup$ ), and green–blue shows the IMAU-FDM or RF densities ( $\rho_{4cm}$ ). The coastline is from Depoorter et al. (2013). (d) shows the relationship between IMAU-FDM or RF densities and SUMup densities. The sizes of the scattered points indicate the time difference between the SUMup measurements and year 2020, and the colour bars show the difference in depth between IMAU-FDM or RF measurements (both fixed at 4 cm) and SUMup measurements ( $d_{FDM} - d_{SUMup}$  and  $d_{RF} - d_{SUMup}$ , respectively).



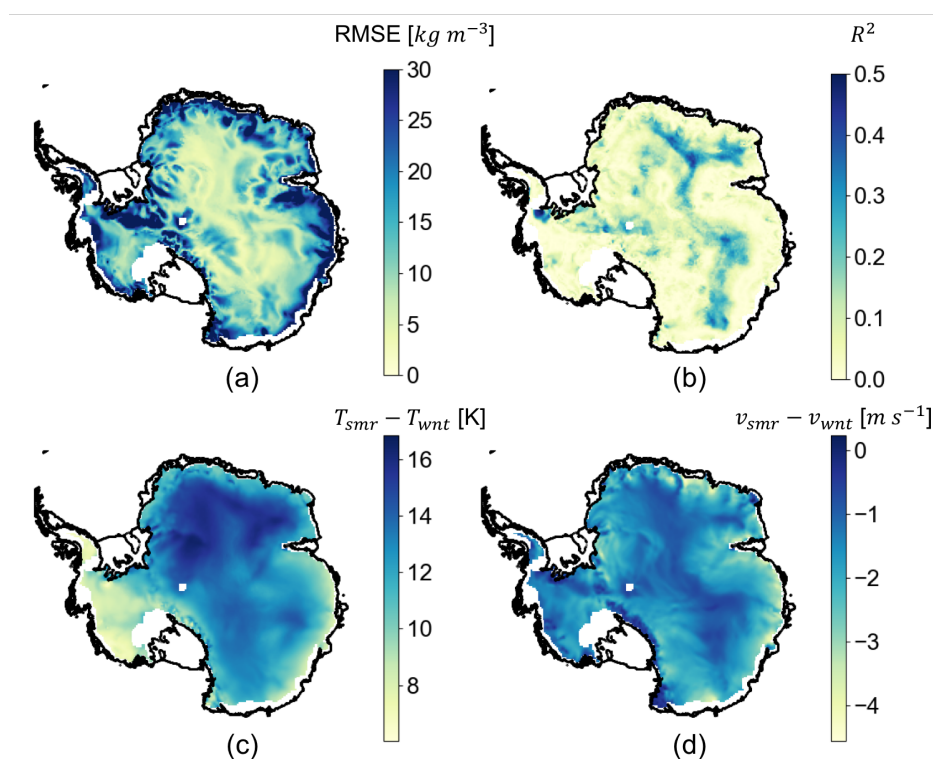


**Figure 7.** Map of (a) root mean square error (RMSE) between IMAU-FDM 4 cm densities and RF densities, (b) coefficient of determination ( $R^2$ ) of the linear fit between IMAU-FDM 4 cm densities and RF densities, (c) the difference between the summer ( $T_{smr}$ ) and winter temperature ( $T_{wnt}$ ) and (d) the difference between the summer ( $v_{smr}$ ) and winter wind velocity ( $v_{wnt}$ ) from ERA5. The coastline is from Depoorter et al. (2013).

regions of East Antarctica and part of West Antarctica. The errors increase towards the coastal regions. The low  $R^2$  values in  
 345 Fig. 6b indicate a low temporal agreement between IMAU-FDM and RF densities. High  $R^2$  values can mainly be observed in  
 high-elevation regions of East Antarctica (except for megadune regions) and a part of West Antarctic Peninsula. The temporal  
 mismatch and low  $R^2$  between IMAU-FDM and RF may be in part due to the modelling errors of IMAU-FDM. The density  
 changes that are not modelled by the IMAU-FDM, but affect the satellite observations, are expected to degrade the quality of  
 the RF regressor. The satellite data might be affected by other climate parameters that are not included in the IMAU-FDM  
 350 model. By assessing the temporal agreement (mainly  $R^2$ ) with ERA5 parameters (Fig. 7c and d), we can learn that a high  
 temporal correspondence is spatially correlated with both a high surface temperature difference ( $> 10K$ ) between Antarctic  
 summer (Oct.–Mar.) and winter (Apr.–Sept.), as well as a small wind velocity difference ( $> -1.5\ m\ s^{-1}$ ) between Antarctic  
 summer and winter.



#### 4.5 Temporal assessment of RF densities at random pixels

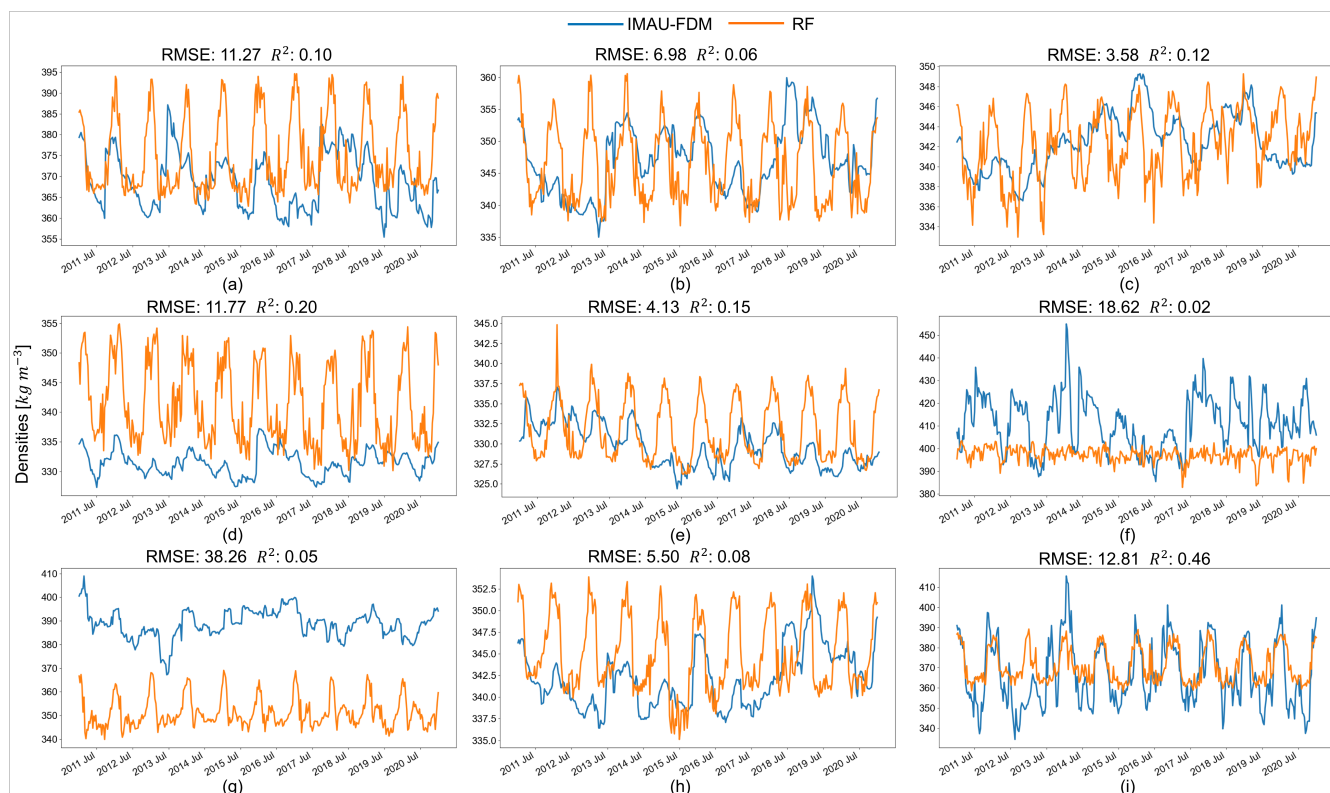


**Figure 8.** Comparison between time series of IMAU-FDM densities (in blue) and RF densities (in orange) at 9 randomly selected sample points. Panels (a)–(i) correspond to A–I labelled in Fig.3. The RMSE and  $R^2$  between the IMAU-FDM densities and the RF densities are shown above each figure.

355 In Figure 8, individual pixels from different clusters are inspected to understand the temporal differences between IMAU-FDM and RF densities. Pixels A–C are selected from cluster Firn 1, pixels D–F belong to Firn 2 (with E referring to Dome C), pixels G and H are from Firn 3, and pixel I is from Firn 4. From the time series, it is apparent that the RF density estimates generally exhibit a stronger and more consistent seasonal cycle compared to the IMAU-FDM densities, which display a less consistent seasonal pattern with stronger inter-annual variations. This discrepancy explains the relatively low  $R^2$  values, as  
360 only the pixels with similar seasonal cycles (e.g., panel I) exhibit a higher correlation between the two datasets.

In Figure 9, a comparison is made between the IMAU-FDM and in situ density measurements at Dome C (pixel E). The PR time series at both frequencies are also provided for comparison, as an increase in PR is theoretically correlated with the formation and removal of the hoar layer, which is characterised by an increased density and a decrease in grain size. The comparison reveals that as the in situ densities vary between approximately  $140 \text{ kg m}^{-3}$  and approximately  $325 \text{ kg m}^{-3}$ ,  
365 the PR values from both frequencies quasi-concurrently vary by approximately 0.04. However, the concurrent IMAU-FDM



densities oscillate between  $327 \text{ kg m}^{-3}$  and  $329 \text{ kg m}^{-3}$ , failing to capture the variation in the hoar layer observed in the in situ densities and the PR time series. This discrepancy between the IMAU-FDM densities and satellite observations can undermine the importance of the PR time series in the RF estimation and subsequently affect the temporal performance of the RF regressor.

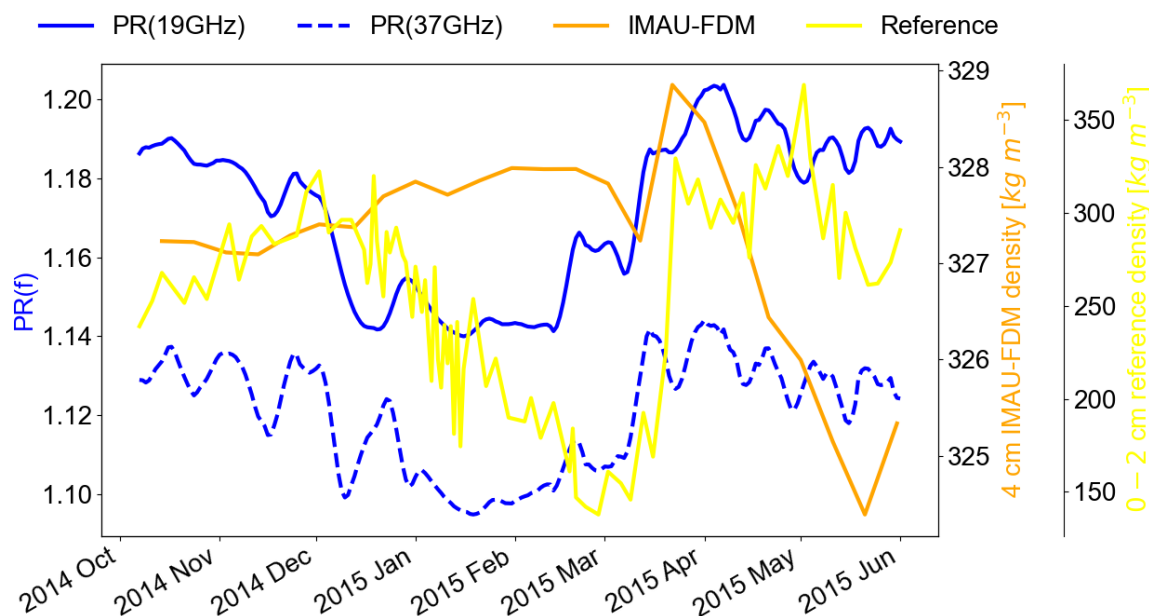


**Figure 9.**  $PR(f)$  (in blue, left axis) with IMAU-FDM densities (in orange, middle axis) and densities from Leduc-Leballeur et al. (2021) (in yellow, right axis).

## 370 5 Discussion

In this study, we developed a novel approach to estimate Antarctic firn densities using satellite radiometer and scatterometer observations using a RF regressor and IMAU-FDM density outputs as reference data. Our findings reveal the complexity of the relationship between satellite parameters and firn density, as well as the limitations of linear models in capturing this relationship. The lack of a consistent linear relationship was evident in both the analysis of different satellite time series clusters and the examination of the individual satellite parameters.

To address the non-linear and complex nature of the relationship between satellite parameters and firn density, we employed a random forest (RF) regressor model. This model allowed us to incorporate multiple input parameters and handle non-linear relationships effectively. The implementation of the RF regressor successfully reproduced the spatial pattern of the IMAU-FDM density, achieving a low root mean square error (RMSE) of  $18.89 \text{ kg m}^{-3}$ . This highlights the potential of using satellite



380 parameters to create a map of long-term mean densities, going beyond the simple reconstruction based on climate drivers as demonstrated by Fraser et al. (2016).

However, it is important to note some limitations and discrepancies in the RF density map. We observed a slight overestimation of densities in the interior of the Antarctic ice sheet, coupled with an underestimation towards the coastal regions, when compared to the IMAU-FDM densities. This discrepancy may arise from the inability of the RF regressor to extrapolate  
385 beyond the training data, leading to the restricted density range in the RF density map (maximum density of  $\leq 410 \text{ kg m}^{-3}$ ). Furthermore, when comparing the RF and IMAU-FDM densities with the in situ SUMup measurements, we found comparable errors. Similar errors were reported by Keenan et al. (2021), who attributed them to local meteorological phenomena not captured by climate models and possible measurement uncertainties. These factors, which are not explicitly accounted for in the IMAU-FDM model or the RF regressor trained on that dataset, may contribute to the discrepancies observed.

390 While the RF regressor successfully captures the spatial variability of the long-term mean density, it falls short in accurately predicting the temporal variation in IMAU-FDM, particularly in coastal regions. The temporal discrepancies between the RF regressor and IMAU-FDM can be attributed to the differences in seasonal patterns and the presence of complex climate conditions near the ice shelves. Coastal regions, characterised by low temperature differences between summer and winter, and large negative differences in wind velocity, exhibit larger temporal discrepancies. These findings suggest that IMAU-FDM  
395 may not capture the seasonal cycle of fresh snow density in these regions with high wind speeds during winter and a relatively small seasonal temperature cycle. The simplicity of how the density of freshly fallen snow is calculated within IMAU-FDM, assuming linear dependencies with wind speed and surface temperature (Veldhuijsen et al., 2023), fails to account for the intricate processes involving crystal size, shape, and riming, which are influenced by temperature and wind speed conditions (Judson and Doesken, 2000). The dependence of fresh snow density on wind speed may differ under various temperature  
400 conditions, which contributes to the discrepancies observed.

In summary, the RF regressor trained using IMAU-FDM and satellite parameters demonstrates promising results in capturing the spatial pattern of firn density. However, it may not fully capture the temporal fluctuations of IMAU-FDM, primarily due to the dominant influence of surface temperature (represented by  $T_B$ ) in the RF estimation. The effects of precipitation (e.g., represented by changes in  $\sigma^0$  Fraser et al., 2016), and wind velocity (e.g., represented by  $PR(f)$  Champollion et al., 2013)  
405 are therefore potentially compromised in the RF model. Additionally, the discrepancy between the meteorological forcing in the IMAU-FDM model and the actual meteorological phenomena can also play a role. The meteorological phenomena can affect the satellite parameters, which in turn influence the RF results, but may not be reflected in the IMAU-FDM output. Our approach of training the RF regressor on IMAU-FDM, which may exhibit spatial and temporal differences compared to actual in situ densities, can therefore be considered a major shortcoming. This limitation should be taken into consideration  
410 when interpreting the RF density estimations. Future research could benefit from incorporating more in situ measurements for training the RF regressor, which would improve the accuracy of the temporal density estimates. Additionally, exploring alternative machine learning algorithms or ensemble approaches may further enhance the performance of density estimation and capture the complex relationships between satellite observations and firn density.



415 Despite the limitations and discrepancies observed, the RF density map generated in this study can serve as an important intermediate step in translating satellite data into density estimations. It provides valuable insights into the discrepancy between firm models and satellite observations, shedding light on the complexities of the relationship between satellite parameters and firm density. The RF regressor captures the long-term mean density pattern, offering a useful tool for investigating spatial variations in firm density across Antarctica. However, it is essential to exercise caution when interpreting the temporal variations, particularly in coastal regions with complex climate conditions.

420 Further improvements can be made to enhance the accuracy of the RF regressor in capturing the temporal variations of firm density. This could involve refining the training data and incorporating additional meteorological parameters that influence the satellite observations. By better accounting for the effects of precipitation and wind velocity on the satellite parameters, the RF regressor could potentially capture a more accurate representation of the temporal dynamics of firm density. Furthermore, advancements in the parameterisation of fresh snow density within firm models, considering the complex processes driven by 425 temperature and wind speed conditions, could help bridge the gap between model predictions and satellite observations.

## 6 Conclusions

In conclusion, this study demonstrates the potential of using multiple satellite observations to estimate Antarctic firm densities, with the IMAU-FDM densities serving as a reference. Our findings highlight several key points. Firstly, while satellite observations exhibit spatial correlations with firm densities, a consistent linear relationship cannot be established. The correlations 430 between  $\rho_{4cm}$  and satellite parameters, particularly  $T_B$  and  $FR(p)$ , indicate their potential influence on firm density variations.

Secondly, the impact of firm melt and refreeze on satellite observations is significant. Temporal anomalies in satellite parameters can be adopted to differentiate between wet and dry firm regions. Clustering of satellite observation time series helps to identify melt extents and assess the temporal correlation with densities at the cluster level. Notably, the scattering impact of refrozen melt layers is reflected in prolonged elevated  $\sigma^0$  anomalies. However, in dry snow clusters, the correlation between 435 densities and satellite observations is not evident.

Based on these complexities, a non-linear model, such as the random forest (RF) regressor, is necessary to capture the relationship between firm densities and satellite observations. Our implementation of the RF regressor successfully reproduces the spatial pattern of firm densities, exhibiting good agreement with IMAU-FDM and even outperforming it in certain locations when compared with SUMup density measurements. However, the temporal simulation of densities by the RF regressor is 440 compromised. Individual pixel analyses reveal that the RF densities tend to overestimate densities in summer when they are in phase with IMAU-FDM densities. In coastal regions, where satellite signals with strong variability dominate, the RF densities are not directly comparable to IMAU-FDM densities. These temporal discrepancies can be attributed to the simplifications in the IMAU-FDM model, particularly in capturing wind and temperature dependencies that strongly influence satellite observations. Furthermore, limitations of the RF regressor, including the inability to extrapolate from the training dataset and 445 its strong dependency on brightness temperatures, result in a limited range of density estimation and primarily reflect surface temperatures.



*Data availability.* The SSMIS data are available at <https://nsidc.org/data/nsidc-0001/versions/6>. The ASCAT Enhanced Resolution Image Products are available at [https://www.scp.byu.edu/data/Ascat/SIR/Ascat\\_sir.html](https://www.scp.byu.edu/data/Ascat/SIR/Ascat_sir.html). The SUMup data are available at <https://arcticdata.io/catalog/view/doi:10.18739/A2ZS2KD0Z>. The ERA5 land hourly data are available at <https://doi.org/10.24381/cds.e2161bac>. The IMAU-  
450 FDM data are available upon request from [s.b.m.veldhuijsen@uu.nl](mailto:s.b.m.veldhuijsen@uu.nl).

*Author contributions.* WL and SL designed the study. WL conducted data management, processing and analysis; produced the figures; and provided the manuscript with contributions from all co-authors. SV processed and provided the IMAU-FDM densities. SL provided support on data visualisation and analysis.

*Competing interests.* Stef Lhermitte is a member of the editorial board of The Cryosphere.

455 *Acknowledgements.* Weiran Li is supported by the Dutch Research Council (NWO) on the ALWGO.2017.033 project. Sanne B. M. Veldhuijsen is supported by the Netherlands Organization for Scientific Research (grantno.OCENW.GROOT.2019.091).

We acknowledge National Snow and Ice Data Center (NSIDC) for providing the SSMIS brightness temperature data, Brigham Young University (BYU) Center for Remote Sensing for providing the ASCAT incidence angle normalised backscatter intensity, ECMWF for providing the ERA5 data, and the Surface Mass Balance and Snow on Sea Ice Working Group (SUMup) and the group of Dr Leduc-Leballeur  
460 for providing the firm density measurements over Antarctica.

ChatGPT is used for grammar checks in parts of the manuscript.



## References

- Archer, K. J. and Kimes, R. V.: Empirical characterization of random forest variable importance measures, *Computational Statistics & Data Analysis*, 52, 2249–2260, <https://doi.org/10.1016/j.csda.2007.08.015>, 2008.
- 465 Breiman, L.: Bagging predictors, *Machine Learning*, 24, 123–140, <https://doi.org/10.1007/bf00058655>, 1996.
- Breiman, L.: Random Forests, *Machine Learning*, 45, 5–32, <https://doi.org/10.1023/a:1010933404324>, 2001.
- Brigham Young University (BYU) Microwave Earth Remote Sensing (MERS) laboratory: Standard BYU ASCAT Land/Ice Image Products, [https://www.scp.byu.edu/data/Ascat/SIR/Ascat\\_sir.html](https://www.scp.byu.edu/data/Ascat/SIR/Ascat_sir.html), [Access date: Feb. 6, 2021], 2010.
- Brucker, L., Picard, G., and Fily, M.: Snow grain-size profiles deduced from microwave snow emissivities in Antarctica, *Journal of Glaciology*, 56, 514–526, <https://doi.org/10.3189/002214310792447806>, 2010.
- 470 Brucker, L., Picard, G., Arnaud, L., Barnola, J.-M., Schneebeli, M., Brunjail, H., Lefebvre, E., and Fily, M.: Modeling time series of microwave brightness temperature at Dome C, Antarctica, using vertically resolved snow temperature and microstructure measurements, *Journal of Glaciology*, 57, 171–182, <https://doi.org/10.3189/002214311795306736>, 2011.
- Brucker, L., Dinnat, E. P., Picard, G., and Champollion, N.: Effect of Snow Surface Metamorphism on Aquarius L-Band
- 475 Radiometer Observations at Dome C, Antarctica, *IEEE Transactions on Geoscience and Remote Sensing*, 52, 7408–7417, <https://doi.org/10.1109/tgrs.2014.2312102>, 2014.
- Champollion, N., Picard, G., Arnaud, L., Lefebvre, E., and Fily, M.: Hoar crystal development and disappearance at Dome C, Antarctica: observation by near-infrared photography and passive microwave satellite, *The Cryosphere*, 7, 1247–1262, <https://doi.org/10.5194/tc-7-1247-2013>, 2013.
- 480 Copernicus Climate Change Service: ERA5-Land hourly data from 2001 to present, <https://doi.org/10.24381/CDS.E2161BAC>, 2019.
- Craven, M. and Allison, I.: Firnification and the effects of wind-packing on Antarctic snow, *Annals of Glaciology*, 27, 239–245, <https://doi.org/10.3189/1998aog27-1-239-245>, 1998.
- de Roda Husman, S., Hu, Z., Wouters, B., Munneke, P. K., Veldhuijsen, S., and Lhermitte, S.: Remote Sensing of Surface Melt on Antarctica: Opportunities and Challenges, *IEEE Journal of Selected Topics in Applied Earth Observations and Remote Sensing*, pp. 1–20,
- 485 <https://doi.org/10.1109/jstars.2022.3216953>, 2022.
- Depoorter, M. A., Bamber, J. L., Griggs, J., Lenaerts, J. T. M., Ligtenberg, S. R. M., van den Broeke, M. R., and Moholdt, G.: Synthesized grounding line and ice shelf mask for Antarctica, <https://doi.org/10.1594/PANGAEA.819151>, supplement to: Depoorter, MA et al. (2013): Calving fluxes and basal melt rates of Antarctic ice shelves. *Nature*, 502, 89–92, <https://doi.org/10.1038/nature12567>, 2013.
- Early, D. and Long, D.: Image reconstruction and enhanced resolution imaging from irregular samples, *IEEE Transactions on Geoscience and Remote Sensing*, 39, 291–302, <https://doi.org/10.1109/36.905237>, 2001.
- 490 Fahnestock, M., Bindschadler, R., Kwok, R., and Jezek, K.: Greenland Ice Sheet Surface Properties and Ice Dynamics from ERS-1 SAR Imagery, *Science*, 262, 1530–1534, <https://doi.org/10.1126/science.262.5139.1530>, 1993.
- Figa-Saldaña, J., Wilson, J. J., Attema, E., Gelsthorpe, R., Drinkwater, M. R., and Stoffelen, A.: The advanced scatterometer (ASCAT) on the meteorological operational (MetOp) platform: A follow on for European wind scatterometers, *Canadian Journal of Remote Sensing*,
- 495 28, 404–412, <https://doi.org/10.5589/m02-035>, 2002.
- Fraser, A. D., Nigro, M. A., Ligtenberg, S. R. M., Legrésy, B., Inoue, M., Cassano, J. J., Kuipers Munneke, P., Lenaerts, J. T. M., Young, N. W., Treverrow, A., van den Broeke, M., and Enomoto, H.: Drivers of ASCAT C band backscatter variability in the dry snow zone of Antarctica, *Journal of Glaciology*, 62, 170–184, <https://doi.org/10.1017/jog.2016.29>, 2016.



- Fujita, S., Goto-Azuma, K., Hirabayashi, M., Hori, A., Iizuka, Y., Motizuki, Y., Motoyama, H., and Takahashi, K.: Densification of layered  
500 firn in the ice sheet at Dome Fuji, Antarctica, *Journal of Glaciology*, 62, 103–123, <https://doi.org/10.1017/jog.2016.16>, 2016.
- Hengl, T., Nussbaum, M., Wright, M. N., Heuvelink, G. B., and Gräler, B.: Random forest as a generic framework for predictive modeling  
of spatial and spatio-temporal variables, *PeerJ*, 6, e5518, <https://doi.org/10.7717/peerj.5518>, 2018.
- Judson, A. and Doesken, N.: Density of Freshly Fallen Snow in the Central Rocky Mountains, *Bulletin of the American Meteorological  
Society*, 81, 1577–1587, [https://doi.org/10.1175/1520-0477\(2000\)081<1577:doffsi>2.3.co;2](https://doi.org/10.1175/1520-0477(2000)081<1577:doffsi>2.3.co;2), 2000.
- 505 Keenan, E., Wever, N., Dattler, M., Lenaerts, J. T. M., Medley, B., Munneke, P. K., and Reijmer, C.: Physics-based SNOWPACK model  
improves representation of near-surface Antarctic snow and firn density, *The Cryosphere*, 15, 1065–1085, <https://doi.org/10.5194/tc-15-1065-2021>, 2021.
- Kingslake, J., Ely, J. C., Das, I., and Bell, R. E.: Widespread movement of meltwater onto and across Antarctic ice shelves, *Nature*, 544,  
349–352, <https://doi.org/10.1038/nature22049>, 2017.
- 510 Koenig, L. and Montgomery, L.: Surface Mass Balance and Snow Depth on Sea Ice Working Group (SUMup) snow density subdataset,  
Greenland and Antarctica, 1950–2018, <https://doi.org/10.18739/A2JH3D23R>, 2018.
- Kuipers Munneke, P., Ligtenberg, S. R. M., Noël, B. P. Y., Howat, I. M., Box, J. E., Mosley-Thompson, E., McConnell, J. R., Steffen, K.,  
Harper, J. T., Das, S. B., and van den Broeke, M. R.: Elevation change of the Greenland Ice Sheet due to surface mass balance and firn  
processes, 1960–2014, *The Cryosphere*, 9, 2009–2025, <https://doi.org/10.5194/tc-9-2009-2015>, 2015.
- 515 Kunkee, D. B., Poe, G. A., Boucher, D. J., Swadley, S. D., Hong, Y., Wessel, J. E., and Uliana, E. A.: Design and Evaluation  
of the First Special Sensor Microwave Imager/Sounder, *IEEE Transactions on Geoscience and Remote Sensing*, 46, 863–883,  
<https://doi.org/10.1109/tgrs.2008.917980>, 2008.
- Leduc-Leballeur, M., Picard, G., Macelloni, G., Arnaud, L., Brogioni, M., Mialon, A., and Kerr, Y.: Influence of snow sur-  
face properties on L-band brightness temperature at Dome C, Antarctica, *Remote Sensing of Environment*, 199, 427–436,  
520 <https://doi.org/https://doi.org/10.1016/j.rse.2017.07.035>, 2017.
- Leduc-Leballeur, M., Picard, G., Macelloni, G., Arnaud, L., Brogioni, M., Mialon, A., and Kerr, Y. H.: Snow density at Dome C, Antarctica  
in 2015, <https://doi.org/10.1594/PANGAEA.934373>, [Access date: Jun. 7, 2022], 2021.
- Lehning, M., Bartelt, P., Brown, B., Fierz, C., and Satyawali, P.: A physical SNOWPACK model for the Swiss avalanche warning: Part II.  
Snow microstructure, *Cold Regions Science and Technology*, 35, 147–167, [https://doi.org/10.1016/s0165-232x\(02\)00073-3](https://doi.org/10.1016/s0165-232x(02)00073-3), 2002.
- 525 Lenaerts, J. T. M., Lhermitte, S., Drews, R., Ligtenberg, S. R. M., Berger, S., Helm, V., Smeets, C. J. P. P., van den Broeke, M. R., van de  
Berg, W. J., van Meijgaard, E., Eijkelboom, M., Eisen, O., and Pattyn, F.: Meltwater produced by wind–albedo interaction stored in an  
East Antarctic ice shelf, *Nature Climate Change*, 7, 58–62, <https://doi.org/10.1038/nclimate3180>, 2016.
- Li, J. and Zwally, H. J.: Modeling the density variation in the shallow firn layer, *Annals of Glaciology*, 38, 309–313,  
<https://doi.org/10.3189/172756404781814988>, 2004.
- 530 Li, W., Lhermitte, S., and López-Dekker, P.: The potential of synthetic aperture radar interferometry for assessing meltwater lake dynamics  
on Antarctic ice shelves, *The Cryosphere*, 15, 5309–5322, <https://doi.org/10.5194/tc-15-5309-2021>, 2021.
- Ligtenberg, S. R. M., Helsen, M. M., and van den Broeke, M. R.: An improved semi-empirical model for the densification of Antarctic firn,  
*The Cryosphere*, 5, 809–819, <https://doi.org/10.5194/tc-5-809-2011>, 2011.
- Lindsley, R. D. and Long, D. G.: Standard BYU ASCAT Land/Ice Image Products, Tech. rep., Brigham Young University Microwave Earth  
535 Remote Sensing (MERS) Laboratory, <https://www.scp.byu.edu/docs/pdf/MERS1002.pdf>, [Access date: Jun. 20, 2022], 2010.





- Long, D. and Drinkwater, M.: Azimuth variation in microwave scatterometer and radiometer data over Antarctica, *IEEE Transactions on Geoscience and Remote Sensing*, 38, 1857–1870, <https://doi.org/10.1109/36.851769>, 2000.
- Long, D., Hardin, P., and Whiting, P.: Resolution enhancement of spaceborne scatterometer data, *IEEE Transactions on Geoscience and Remote Sensing*, 31, 700–715, <https://doi.org/10.1109/36.225536>, 1993.
- 540 Macelloni, G., Brogioni, M., Pampaloni, P., and Cagnati, A.: Multifrequency Microwave Emission From the Dome-C Area on the East Antarctic Plateau: Temporal and Spatial Variability, *IEEE Transactions on Geoscience and Remote Sensing*, 45, 2029–2039, <https://doi.org/10.1109/tgrs.2007.890805>, 2007.
- Meier, W. N., Stewart, J. S., Wilcox, H., Scott, D. J., and Hardman, M. A.: DMSPP SSM/I-SSMIS Daily Polar Gridded Brightness Temperatures, Boulder, Colorado USA. NASA National Snow and Ice Data Center Distributed Active Archive Center, <https://doi.org/10.5067/MXJL42WSXTS1>, [Date Accessed: Mar. 15, 2021], 2021.
- 545 Meredith, M., Sommerkorn, M., Cassotta, S., Derksen, C., Ekaykin, A., Hollowed, A., Kofinas, G., Mackintosh, A., Melbourne-Thomas, J., Muelbert, M., Ottersen, G., Pritchard, H., and Schuur, E.: Polar Regions, chap. 3, pp. 203–320, Cambridge University Press, Cambridge, UK and New York, NY, USA, <https://doi.org/10.1017/9781009157964.005>, 2019.
- Montgomery, L., Koenig, L., and Alexander, P.: The SUMup dataset: compiled measurements of surface mass balance components over ice sheets and sea ice with analysis over Greenland, *Earth System Science Data*, 10, 1959–1985, <https://doi.org/10.5194/essd-10-1959-2018>, 2018.
- 550 Nicolas, J. P., Vogelmann, A. M., Scott, R. C., Wilson, A. B., Cadet, M. P., Bromwich, D. H., Verlinde, J., Lubin, D., Russell, L. M., Jenkinson, C., Powers, H. H., Ryzczek, M., Stone, G., and Wille, J. D.: January 2016 extensive summer melt in West Antarctica favoured by strong El Niño, *Nature Communications*, 8, <https://doi.org/10.1038/ncomms15799>, 2017.
- 555 Picard, G., Fily, M., and Gallee, H.: Surface melting derived from microwave radiometers: a climatic indicator in Antarctica, *Annals of Glaciology*, 46, 29–34, <https://doi.org/10.3189/172756407782871684>, 2007.
- Picard, G., Brucker, L., Fily, M., Gallée, H., and Krinner, G.: Modeling time series of microwave brightness temperature in Antarctica, *Journal of Glaciology*, 55, 537–551, <https://doi.org/10.3189/002214309788816678>, 2009.
- Picard, G., Domine, F., Krinner, G., Arnaud, L., and Lefebvre, E.: Inhibition of the positive snow-albedo feedback by precipitation in interior Antarctica, *Nature Climate Change*, 2, 795–798, <https://doi.org/10.1038/nclimate1590>, 2012.
- 560 Rignot, E.: Mass balance of East Antarctic glaciers and ice shelves from satellite data, *Annals of Glaciology*, 34, 217–227, <https://doi.org/10.3189/172756402781817419>, 2002.
- Rizzoli, P., Martone, M., Rott, H., and Moreira, A.: Characterization of Snow Facies on the Greenland Ice Sheet Observed by TanDEM-X Interferometric SAR Data, *Remote Sensing*, 9, <https://doi.org/10.3390/rs9040315>, 2017.
- 565 Schröder, L., Horwath, M., Dietrich, R., Helm, V., van den Broeke, M. R., and Ligtenberg, S. R. M.: Four decades of Antarctic surface elevation changes from multi-mission satellite altimetry, *The Cryosphere*, 13, 427–449, <https://doi.org/10.5194/tc-13-427-2019>, 2019.
- Spergel, J. J., Kingslake, J., Creyts, T., van Wessem, M., and Fricker, H. A.: Surface meltwater drainage and ponding on Amery Ice Shelf, East Antarctica, 1973–2019, *Journal of Glaciology*, p. 1–14, <https://doi.org/10.1017/jog.2021.46>, 2021.
- Sugiyama, S., Enomoto, H., Fujita, S., Fukui, K., Nakazawa, F., Holmlund, P., and Surdyk, S.: Snow density along the route traversed by the Japanese-Swedish Antarctic Expedition 2007/08, *Journal of Glaciology*, 58, 529–539, <https://doi.org/10.3189/2012jog11j201>, 2012.
- 570 Surdyk, S.: Using microwave brightness temperature to detect short-term surface air temperature changes in Antarctica: An analytical approach, *Remote Sensing of Environment*, 80, 256–271, [https://doi.org/10.1016/s0034-4257\(01\)00308-x](https://doi.org/10.1016/s0034-4257(01)00308-x), 2002.



- Tedesco, M.: Assessment and development of snowmelt retrieval algorithms over Antarctica from K-band spaceborne brightness temperature (1979–2008), *Remote Sensing of Environment*, 113, 979–997, <https://doi.org/10.1016/j.rse.2009.01.009>, 2009.
- 575 Tedesco, M. and Kim, E.: Retrieval of dry-snow parameters from microwave radiometric data using a dense-medium model and genetic algorithms, *IEEE Transactions on Geoscience and Remote Sensing*, 44, 2143–2151, <https://doi.org/10.1109/tgrs.2006.872087>, 2006.
- Tran, N., Remy, F., Feng, H., and Femenias, P.: Snow Facies Over Ice Sheets Derived From Envisat Active and Passive Observations, *IEEE Transactions on Geoscience and Remote Sensing*, 46, 3694–3708, <https://doi.org/10.1109/tgrs.2008.2000818>, 2008.
- van den Broeke, M.: Depth and Density of the Antarctic Firn Layer, *Arctic, Antarctic, and Alpine Research*, 40, 432–438, 580 [https://doi.org/10.1657/1523-0430\(07-021\)\[broeke\]2.0.co;2](https://doi.org/10.1657/1523-0430(07-021)[broeke]2.0.co;2), 2008.
- van den Broeke, M. R., Winther, J.-G., Isaksson, E., Pinglot, J. F., Karlöf, L., Eiken, T., and Conrads, L.: Climate variables along a traverse line in Dronning Maud Land, East Antarctica, *Journal of Glaciology*, 45, 295–302, <https://doi.org/10.3189/s002214300001799>, 1999.
- van Wessem, J. M., van de Berg, W. J., Noël, B. P. Y., van Meijgaard, E., Amory, C., Birnbaum, G., Jakobs, C. L., Krüger, K., Lenaerts, J. T. M., Lhermitte, S., Ligtenberg, S. R. M., Medley, B., Reijmer, C. H., van Tricht, K., Trusel, L. D., van Uft, L. H., Wouters, B., Wuite, 585 J., and van den Broeke, M. R.: Modelling the climate and surface mass balance of polar ice sheets using RACMO2 – Part 2: Antarctica (1979–2016), *The Cryosphere*, 12, 1479–1498, <https://doi.org/10.5194/tc-12-1479-2018>, 2018.
- Veldhuijsen, S. B. M., van de Berg, W. J., Brils, M., Munneke, P. K., and van den Broeke, M. R.: Characteristics of the 1979–2020 Antarctic firn layer simulated with IMAU-FDM v1.2A, *The Cryosphere*, 17, 1675–1696, <https://doi.org/10.5194/tc-17-1675-2023>, 2023.
- Verjans, V., Leeson, A. A., Nemeth, C., Stevens, C. M., Kuipers Munneke, P., Noël, B., and van Wessem, J. M.: Bayesian calibration of firn 590 densification models, *The Cryosphere*, 14, 3017–3032, <https://doi.org/10.5194/tc-14-3017-2020>, 2020.
- Ward, Jr., J. H.: Hierarchical Grouping to Optimize an Objective Function, *Journal of the American Statistical Association*, 58, 236–244, <https://doi.org/10.1080/01621459.1963.10500845>, 1963.
- Zwally, H. J., Giovinetto, M. B., Li, J., Cornejo, H. G., Beckley, M. A., Brenner, A. C., Saba, J. L., and Yi, D.: Mass changes of the Greenland and Antarctic ice sheets and shelves and contributions to sea-level rise: 1992–2002, *Journal of Glaciology*, 51, 509–527, 595 <https://doi.org/10.3189/172756505781829007>, 2005.